Generalized N-State Random Pulse Position Discontinuous PWM for High-Frequency Harmonics Reduction and Performance Improvement at High Modulation Ratios

Peiran Zhang, Shanming Wang, *Senior Member, IEEE*, and Yituo Li

***Abstract*—In previous studies, generalized N-state random pulse position space vector pulsewidth modulation (GNSRPP-SVPWM) has been verified to significantly disperse dominant high-frequency PWM harmonics with constant sampling frequency. However, due to the short durations of zero-voltage vectors at high modulation ratios, SVPWM with two equally distributed zero-voltage vectors is inferior than discontinuous PWM (DPWM) with one zero-voltage vector in reducing harmonic distortion and switching power losses. Therefore, to significantly disperse dominant high-frequency PWM harmonics, reduce harmonic distortion and improve inverter performance, this article proposed GNSRPP-DPWM, which is more advantageous than other random PWM (RPWM) strategies at high modulation ratios. In addition, by avoiding the switching operations of the phase with higher phase current magnitude, GNSRPP-DPWM further reduces switching power losses. At the same time, GNSRPP-DPWM maintains constant sampling frequency, thus not affecting the closed-loop control system. Mathematical analysis, simulations and experiments all verify the effectiveness and advantages of the proposed GNSRPP-DPWM.**

***Index Terms*—Constant sampling frequency, discontinuous pulsewidth modulation (DPWM), harmonic reduction, inverter performance, random pulse position.**

I. INTRODUCTION

PULSEWIDTH modulation (PWM) technology is widely employed in voltage source inverters (VSIs) to enhance both static and dynamic performances [1]. With increasing relevance in daily life, PWM-controlled VSIs find extensive application in areas including AC motor drives, active power filter, static var generation, grid-tied photovoltaic systems, renewable energy conversion [2], [3].

Space vector PWM (SVPWM) with two equally distributed zero-voltage vectors (V_0 and V_7) and six switching operations during each carrier period is recognized as the low-harmonic-distortion modulation strategy [4]. However, due to the short time durations of zero-voltage vectors, narrow pulses will be generated at high modulation ratios. To make the situation worse, the equal distribution of the two zero-voltage vectors further shortens the narrow pulses.

Discontinuous PWM (DPWM) strategies with four switching operations during each carrier period offer considerable advantages at high modulation ratios [5]. DPWM uses only one selected zero-voltage vector per carrier period by either: connecting the phase leg with the maximum duty cycle to the upper dc rail for the entire carrier period (DPWMMAX) or connecting the phase leg with the minimum duty cycle to the lower dc rail for the entire carrier period (DPWMMIN). Compared with SVPWM, these strategies eliminate two switching operations per carrier period, enabling a nominal value of 3/2 increase in switching frequency for the same inverter losses [5]. Based on the principle that the zero-voltage vector to be eliminated is the vector which introduces more switching losses, many DPWM strategies have been discussed in detail to further reduce switching power losses [6], [7], [8].

Nevertheless, both SVPWM and DPWM generate high-frequency dominant PWM harmonic peaks, which will lead to high-frequency current ripple [9], high-frequency electromagnetic vibration and noise [10], [11], [12], strong electromagnetic interference [13], [14] and other problems.

Random PWM (RPWM) strategy effectively addresses the issues discussed above without additional costs. Compared to fixed carrier frequency RPWM (FCF-RPWM), random carrier frequency PWM (RCF-PWM) exhibits superior harmonic dispersion [15], [16]. In recent years, Xu et al. [17] and Bu et al. [18] optimize the probability density distribution function for RCF-PWM to further suppress the PWM harmonics. Besides, periodic carrier frequency PWM is used to optimize the periodic profiles [19], and solve NVH problems of VSI-fed electrical machine [20]. In [21], to suppress the PWM harmonics near the first and second carrier frequencies, Markov chain is applied to RCF-PWM, and the vectors order is also adjusted. In [22], changes in the shape of the triangular carrier wave, along with random carrier frequencies and pulse centers, are implemented while maintaining a constant duty cycle. Bu et al. [23] have

Manuscript received 23 January 2024; revised 22 May 2024; accepted 6 July 2024. Date of publication 11 July 2024; date of current version 4 September 2024. Recommended for publication by Associate Editor K. Akatsu. *(Corresponding author: Shanming Wang.)*

The authors are with the State Key Laboratory of Control and Simulation of Power System and Generation Equipment, Department of Electrical Engineering, Tsinghua University, Beijing 100084, China (e-mail: zpr23@mails.tsinghua.edu.cn; wangsm96@mails.tsinghua.edu.cn; liyituo@mail.tsinghua.edu.cn).

Color versions of one or more figures in this article are available at https://doi.org/10.1109/TPEL.2024.3426564.

Digital Object Identifier 10.1109/TPEL.2024.3426564

partitioned the frequency range to more effectively reduce high-frequency PWM harmonics.

However, in closed-loop digitally controlled system, using RCF-PWM strategies, which involve variable carrier frequencies, will lead to variable sampling frequencies, potentially deteriorating the performance of the closed-loop systems [23], [24], [25].

FCF-RPWM strategies, characterized by fixed carrier frequency and fixed sampling frequency, are appropriate for closed-loop control systems. However, traditional FCF-RPWM techniques, such as random lead-lag PWM, random center displacement PWM (RCD-PWM), and random zero vector distribution PWM (RZD-PWM), exhibit poor harmonic suppression performance [26], [27], [28]. To significantly improve the harmonic dispersion performance of FCF-RPWM, Zhang et al. [29] proposed *N*-state random pulse position SVPWM (NSRPP-SVPWM), which effectively disperses dominant discrete PWM harmonic peaks. Nevertheless, this approach will result in simultaneous multi-phase switching operations, which should be avoided in practical applications due to associated noise, nuisance trips, strong interference, and instantaneous line-to-line voltage reversals [30], [31], [32], [33]. Therefore, generalized NSRPP-SVPWM (GNSRPP-SVPWM) proposed in [34] mitigates these issues by eliminating simultaneous multi-phase switching operations and significantly reducing extra switching counts (ESCs) without impacting the performance of PWM harmonic dispersion. However, GNSRPP-SVPWM suffers the defect of short durations of the two zero-voltage vectors at high modulation ratios, which makes it natural to associate that one zero-voltage vector should be eliminated at high modulation ratios to further improve the inverter performance.

Combining DPWM with random strategy to significantly disperse PWM harmonics while taking full advantage of DPWM at high modulation ratios is currently a gap, which is the motivation and goal of this article. In this article, GNSRPP-DPWM is introduced, analyzed and compared with other RPWM strategies to show its advantages at high modulation ratios. The working process of the proposed GNSRPP-DPWM is divided into three steps. First, the zero-voltage vector that introduces more switching losses is eliminated. Then, the corresponding fundamental carrier patterns are determined. Finally, one of the *N* fundamental carrier patterns is randomly selected for each carrier period.

Theoretical analysis, simulation and experiment all confirm the advantages of the proposed GNSRPP-DPWM at high modulation ratios in four aspects. First, it effectively reduces the dominant PWM harmonic peaks, with the exception of those close to the *N*th carrier frequency and its multiples. Second, GNSRPP-DPWM maintains constant sampling frequency, which makes it applicable in closed-loop control systems. Third, simultaneous multiphase switching operations are completely avoided. Fourth, compared with other RPWM strategies, the proposed GNSRPP-DPWM has lower switching power losses, lower phase current total harmonic distortion (THD) and better inverter performance at high modulation ratios.

The rest of this article is organized as follows. In Section II, the advantages of DPWM at high modulation ratios are introduced and explained. Section III reviews the traditional RPWM strategies. In Section IV, reference waves, working process, design of fundamental carrier patterns and PWM harmonics dispersion principle of the proposed strategies are introduced. Simulation results are shown in Section V. Experiments are conducted in Section VI. Finally, Section VII concludes this article.

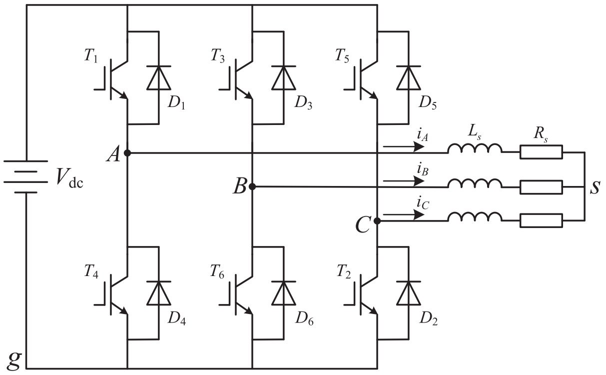

Fig. 1. Traditional three-phase two-level voltage source inverter.

II. ADVANTAGES OF DPWM AT HIGH MODULATION RATIOS

As shown in Fig. 1, the topology of the tested converter is a three-phase two-level inverter, which is widely used in industrial applications. In the differential-mode domain, three-phase voltages (V_{As}, V_{Bs}, and V_{Cs}) determine three-phase currents (i_A, i_B, and i_C), and are defined by the three-phase output PWM pulses (V_{Ag}, V_{Bg}, and V_{Cg}) as follows:

$$
\begin{aligned}
V_{As} &= \frac{1}{3}\left(2V_{Ag} - V_{Bg} - V_{Cg}\right) \\
V_{Bs} &= \frac{1}{3}\left(2V_{Bg} - V_{Ag} - V_{Cg}\right) \\
V_{Cs} &= \frac{1}{3}\left(2V_{Cg} - V_{Ag} - V_{Bg}\right). \qquad (1)
\end{aligned}
$$

Fig. 2 illustrates the three-phase output PWM pulses and the corresponding three-phase currents for conventional SVPWM, DPWMMAX and DPWMMIN at a high modulation ratio. And the carrier period of conventional SVPWM is 1.5 times that of DPWM. It is evident that the phase current ripple of DPWMMAX or DPWMMIN is smaller than that of conventional SVPWM. This is due to the short durations of zero-voltage vectors, segmenting active space vectors is more advantageous than segmenting zero-voltage vectors in reducing harmonic distortion. The work in [5] proves by mathematical analysis that when the modulation ratio is larger than 0.75, DPWM strategies become more advantageous than SVPWM in reducing harmonic distortion.

Moreover, it can be seen that DPWMMAX can avoid the switching operations of the phase with the maximum duty cycle, and DPWMMIN can avoid the switching operations of the phase with the minimum duty cycle.

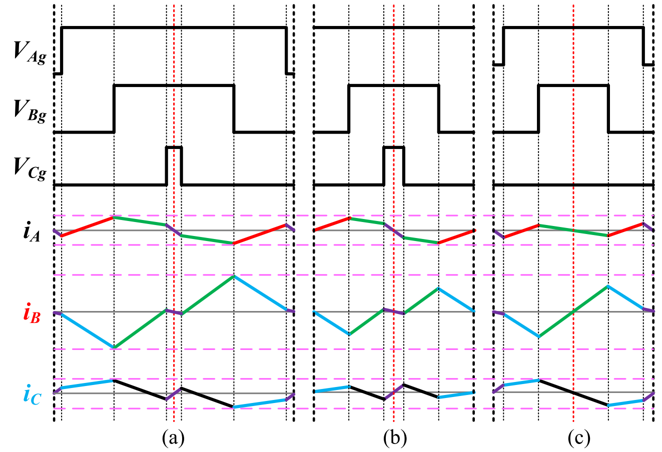

Fig. 2. Illustration of three-phase output PWM pulses and the corresponding three-phase currents for (a) conventional SVPWM, (b) DPWMMAX, and (c) DPWMMIN.

DPWMMAX and DPWMMIN can be used alternately according to power factor angle or phase current magnitude comparison to avoid the switching operations with more switching losses. In a closed-loop control system, three-phase currents are sampled to conduct closed-loop control. Therefore, this article adopts the method of phase current magnitude comparison.

III. Review of the Traditional RPWM Strategies

As shown in Fig. 3(a), for RCF-PWM, the carrier period T_s is selected randomly within a defined range (T_{r1}, T_{r2}). And the probability density distribution function can be introduced to further reduce the PWM harmonics. However, because the control algorithm synchronizes with the carrier period, the variable current sampling frequency deteriorates the closed-loop system performance.

As shown in Fig. 3(b), for RCD-PWM, the three-phase output PWM pulses share the same carrier, are aligned at the center, and their central position is randomly shifted by T_{RCD} from the midpoint of the carrier period. It is crucial to ensure that the three-phase output PWM pulses do not exceed the boundaries of the carrier period.

As shown in Fig. 3(c), for RZD-PWM, the three-phase output PWM pulses share the same carrier, are center-aligned at the midpoint of the carrier period, and the ratio between the durations of the two zero-voltage vectors, $V_0(000)$ and $V_7(111)$, is randomized.

Obviously, the PWM harmonic reduction effect of both RCD-PWM and RZD-PWM is limited by the short durations of zero-voltage vectors.

As illustrated in Fig. 4, 4SRPP-SVPWM is taken as an example of NSRPP-SVPWM to illustrate. By randomly selecting one of the four carrier patterns with the carrier phase shift angles of “0”, “$\pi/2$”, “π,” and “$3\pi/2$” for each carrier period, the carrier wave intersects the three-phase phase reference waves VR_A, VR_B, and VR_C to generate the three-phase output PWM pulses. While 4SRPP-SVPWM effectively disperses dominant PWM harmonics and maintains a constant sampling frequency, it also leads to simultaneous multiphase switching operations at the carrier period boundaries, as shown in Fig. 4.

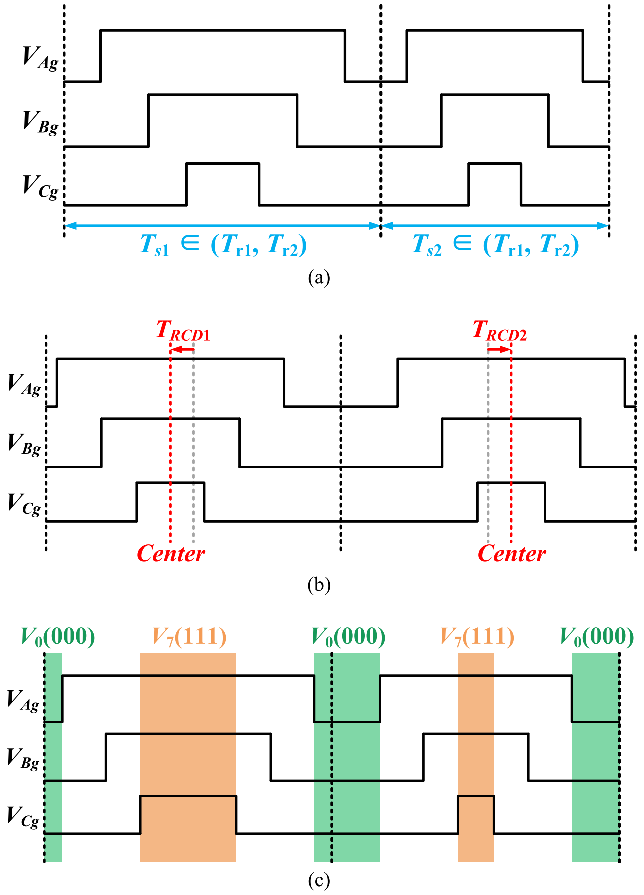

Fig. 3. Illustration of traditional RPWM strategies. (a) Random carrier frequency PWM. (b) Random center displacement PWM. (c) Random zero vector distribution PWM.

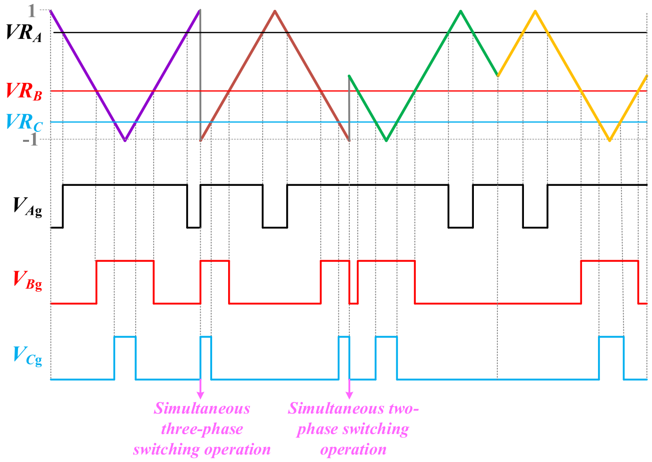

Fig. 4. Working process of 4SRPP-SVPWM.

Therefore, GNSRPP-SVPWM is introduced to address the shortcomings of NSRPP-SVPWM. Illustrated in Fig. 5 with G4SRPP-SVPWM as an example, this approach sets the carrier phase shift angles of the four carrier patterns to “$\pi/4$”, “$3\pi/4$”,

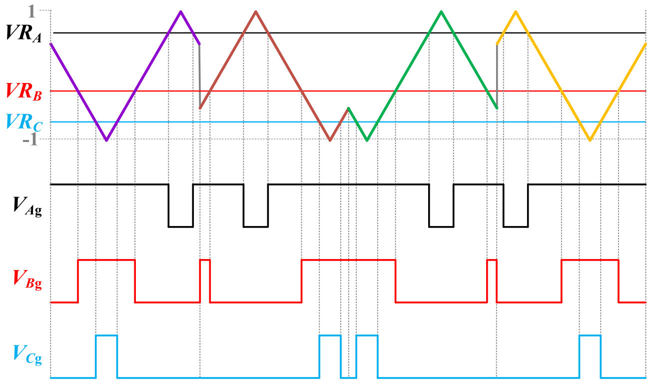

Fig. 5. Working process of G4SRPP-SVPWM.

"$5\pi/4$," and "$7\pi/4$". This configuration effectively prevents simultaneous multiphase switching operations, with only the phase having the medium duty cycle potentially introducing ESCs.

However, at high modulation ratios, the short durations of zero-voltage vectors constrain the performance of GNSRPP-SVPWM. Thus, this article is dedicated to combining DPWM with RPWM and takes full advantage of DPWM at high modulation ratios.

IV. INTRODUCTION AND ANALYSIS OF THE PROPOSED GNSRPP-DPWM

A. Three-Phase Reference Waves

The normalized three-phase voltages are defined as VN_A, VN_B and VN_C, and they meet

$$\begin{aligned} VN_A(t) &= \frac{2}{\sqrt{3}} a \cdot \cos(\omega_0 t) \\ VN_B(t) &= VN_A\left(t - \frac{2}{3}\pi\right) \\ VN_C(t) &= VN_A\left(t + \frac{2}{3}\pi\right) \end{aligned} \tag{2}$$

where ω_0 is the angular frequency of fundamental component, and the modulation ratio a is defined as

$$a = \frac{\sqrt{3}}{V_{\mathrm{dc}}} |V_{As\_\mathrm{fun}}| \tag{3}$$

where $|V_{As\_\mathrm{fun}}|$ refers to the amplitude of the fundamental phase voltage, V_{dc} denotes the dc-link voltage and $0 \leq a \leq 1$.

Define the duty cycle as

$$D_{ph}(t) = 0.5 \cdot (VN_{ph}(t) + VN_0(t)) + 0.5 \tag{4}$$

where $ph = A, B,$ or C for three phases. VN_0 is the zero-sequence voltage injected into the normalized three-phase voltages. In the following description, $D_{\max}$ and $D_{\min}$ are the maximum and minimum duty cycles, respectively. And $VN_{\max}$, VN_{mid}, and $VN_{\min}$ are the maximum, medium and minimum values of the normalized three-phase voltages.

When utilizing only the zero-voltage vector $V_0(000)$, the resulting injected zero-sequence voltage with "$D_{\min}(t) = 0$" is determined to be "$VN_0(t) = -1 - VN_{\min}(t)$." Conversely, when the zero-voltage vector $V_7(111)$ is the only one used, the injected zero-sequence voltage with "$D_{\max}(t) = 1$" is calculated as "$VN_0(t) = 1 - VN_{\max}(t)$." Consequently, the A-phase reference waves of DPWMMAX and DPWMMIN are expressed as

$$VR_{\mathrm{DPWMMAX}\_A}(t) = \frac{2}{\sqrt{3}} a \cdot \cos(\omega_0 t) + (1 - VN_{\max}(t)) \tag{5}$$

$$VR_{\mathrm{DPWMMIN}\_A}(t) = \frac{2}{\sqrt{3}} a \cdot \cos(\omega_0 t) + (-1 - VN_{\min}(t)). \tag{6}$$

The proposed random strategies only change the output PWM pulse positions, while the reference waves remain as shown in (5) and (6).

In closed-loop control systems, three-phase currents are sampled every carrier period. GNSRPP-DPWM first compares the phase current magnitudes of the phases with the maximum and minimum duty cycles, and then decides whether to use DPWMMAX or DPWMMIN to avoid the switching operations with more switching losses. Therefore, for the proposed GNSRPP-DPWM, the injected zero-sequence voltage is expressed as

$$VN_{\mathrm{GNSRPP-DPWM\_0}}(t) = \begin{cases} 1 - VN_{\max}(t), & |i_{D\max}(t)| \geq |i_{D\min}(t)| \\ -1 - VN_{\min}(t), & |i_{D\max}(t)| < |i_{D\min}(t)| \end{cases} \tag{7}$$

where $|i_{D\max}|$ and $|i_{D\min}|$ denote the phase current magnitudes with the maximum and minimum duty cycles, respectively.

Then, the A-phase reference wave of the proposed GNSRPP-DPWM is expressed as

$$VR_{\mathrm{GNSRPP-DPWM\_}A}(t) = \begin{cases} \frac{2}{\sqrt{3}} a \cdot \cos(\omega_0 t) + (1 - VN_{\max}(t)), \\ |i_{D\max}(t)| \geq |i_{D\min}(t)| \\ \frac{2}{\sqrt{3}} a \cdot \cos(\omega_0 t) + (-1 - VN_{\min}(t)), \\ |i_{D\max}(t)| < |i_{D\min}(t)| \end{cases}. \tag{8}$$

B. Working Process

The proposed strategy features N fundamental carrier patterns available for random selection. As depicted in Fig. 6(a) and (b), the operational process relies on a random number generator to select randomly from these N patterns with equal probability during each carrier period.

C. Design of Fundamental Carrier Patterns

G3SRPP-DPWM and G4SRPP-DPWM are taken as examples of the proposed GNSRPP-DPWM to analyze. Then, other GNSRPP-DPWM with odd integer N can be derived by analogy from G3SRPP-DPWM. And other GNSRPP-DPWM with even integer N can be derived by analogy from G4SRPP-DPWM.

1) G4SRPP-DPWM: Fig. 7 demonstrates that in the proposed G4SRPP-DPWM method, the phase-shift angles of the

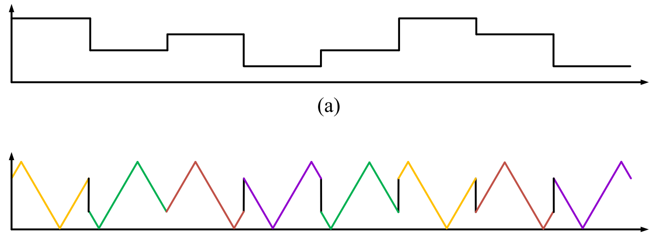
(a)

(b)

Fig. 6. Process for random carrier pattern selection. (a) Random number generation. (b) Carrier wave.

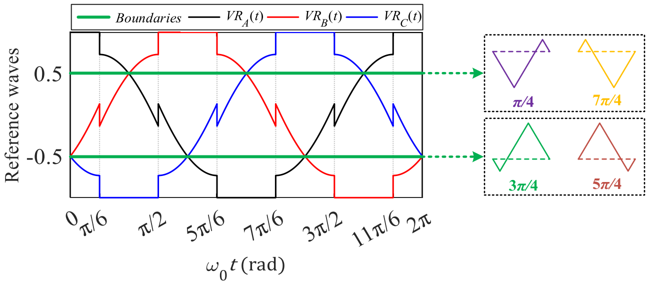

Fig. 7. Three-phase reference waves and possible boundary values of various fundamental carrier patterns for G4SRPP-DPWM with the modulation ratio $a = \frac{\sqrt{3}}{2}$ and unity power factor load.

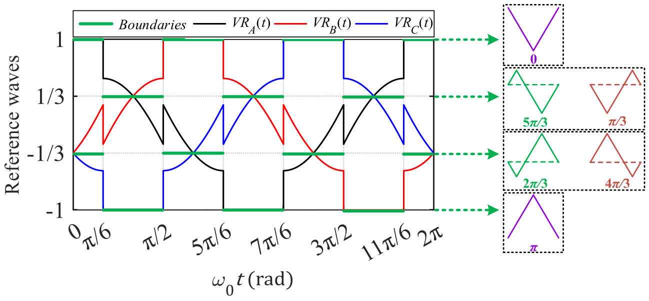

Fig. 8. Three-phase reference waves and possible boundary values of various fundamental carrier patterns for G3SRPP-DPWM with the modulation ratio $a = \frac{4}{3\sqrt{3}}$ and unity power factor load.

four fundamental carrier patterns are set to "$\pi/4$", "$3\pi/4$", "$5\pi/4$," and "$7\pi/4$" with the corresponding boundary values of "0.5", "-0.5", "-0.5," and "0.5." Each pair of them is separated by a phase-shift angle of $\pi/2$ or its multiples.

When it satisfies that "$VR_{\text{DPWMMAX\_}A}(0) \leq -1/2$" or "$VR_{\text{DPWMMIN\_}A}(0) \geq 1/2$", i.e., $a \geq \frac{\sqrt{3}}{2}$, the reference wave values for two phases consistently higher or lower than all boundary values of the four fundamental carrier patterns, as shown in Fig. 7. This effectively eliminates the possibility of simultaneous multiphase switching operations.

2) G3SRPP-DPWM: As shown in Fig. 8, for the proposed G3SRPP-DPWM, there are two cases.

Case 1: When it satisfies that "$VN_0(t) = 1 - VN_{\max}(t)$," the phase-shift angles of the three fundamental carrier patterns

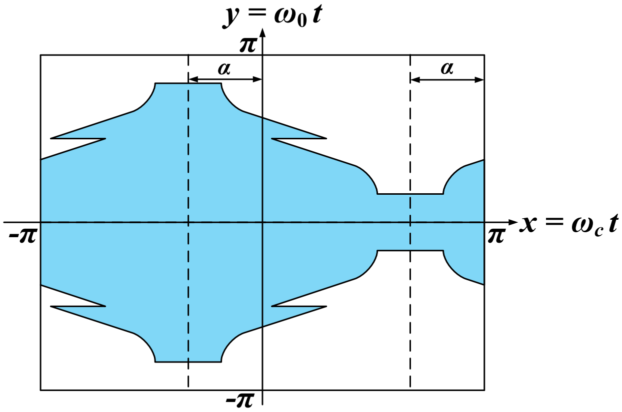

Fig. 9. Unit cell for double Fourier integral with unity power factor load and the carrier phase shift angle of α.

are set to "0", "$2\pi/3$," and "$4\pi/3$", with the corresponding boundary values of "1", "$-1/3$," and "$-1/3$".

Case 2: When it satisfies that "$VN_0(t) = -1 - VN_{\min}(t)$", the phase-shift angles of the three fundamental carrier patterns are set to "$\pi/3$", "π," and "$5\pi/3$," with the corresponding boundary values of "1/3", "-1," and "1/3."

For both cases, there is a carrier phase shift angle of $2\pi/3$ between each pair of the three fundamental carrier patterns.

When it satisfies that "$VR_{\text{DPWMMAX\_}A}(0) \leq -1/3$" or "$VR_{\text{DPWMMIN\_}A}(0) \geq 1/3$", i.e., $a \geq \frac{4}{3\sqrt{3}}$, the reference wave values for two phases consistently higher or lower than all boundary values of the three fundamental carrier patterns, as shown in Fig. 8. This effectively eliminates the possibility of simultaneous multiphase switching operations.

D. PWM Harmonics Dispersion Principle

Two-dimensional Fourier analysis is used to conduct PWM harmonic analysis. This method maps time t to two dimensions: the carrier period ($x = 2\pi f_c t = \omega_c t$) and the modulating function period ($y = 2\pi f_o t = \omega_o t$). The output PWM pulse, which varies over time, is characterized by its PWM harmonic components as follows:

$$V_{Ag}(t) = \frac{V_{dc}}{2} + \sum_{n=1}^{\infty}\left[A_{0n}\cos(n\omega_0 t) + B_{0n}\sin(n\omega_0 t)\right] + \sum_{m=1}^{\infty}\sum_{n=-\infty}^{\infty}\left[A_{mn}\cos(m\omega_c t + n\omega_0 t) + B_{mn}\sin(m\omega_c t + n\omega_0 t)\right] \tag{9}$$

where m represents the carrier index, n denotes the baseband index, A_{mn} and B_{mn} refer to the PWM harmonic amplitudes, and ω_c denotes the angular carrier frequency.

The unit cell for double Fourier integral with unity power factor load and the carrier phase shift angle of α is shown in Fig. 9. Thus, naturally sampled modulation yields the following

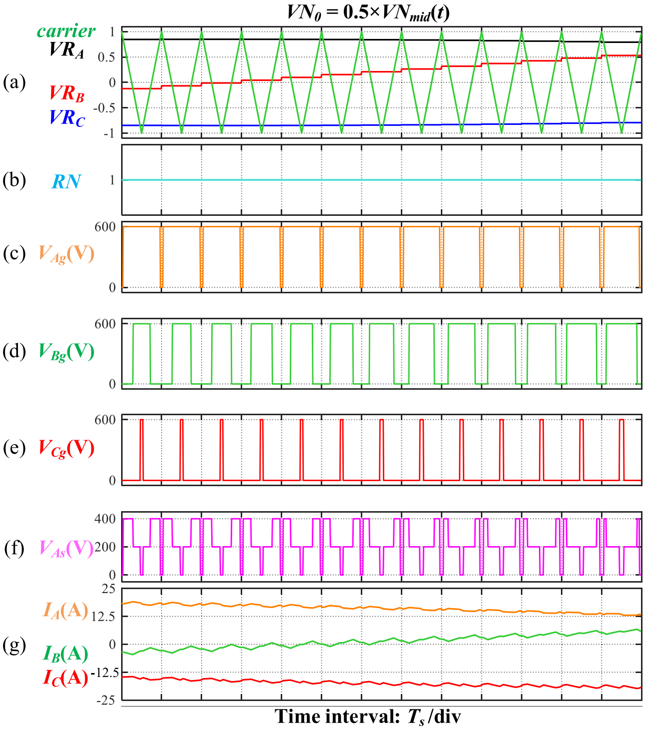

Fig. 10. Simulated waveforms when using the conventional SVPWM with the modulation ratio $a = 0.85$ and the carrier frequency $f_c = 10$ kHz. (a) Intersection between carrier and three-phase reference waves. (b) Random number. (c) *A*-phase output PWM pulse. (d) *B*-phase output PWM pulse. (e) *C*-phase output PWM pulse. (f) *A*-phase voltage. (g) Three-phase currents.

TABLE I

Parameters of Simulation Background

Parameters	Value
DC-link voltage	600 V
Modulation ratio	0.85
Carrier frequency	10 kHz
Fundamental frequency	60 Hz
RL load	$R = 15\Omega$, $L = 3\ mH$
Power factor angle	4.31°

TABLE II

Switching Power Losses and Phase Current THD of Different Strategies

Modulation Strategies	Switching Power Losses	Phase Current THD
Conventional SVPWM, f_c = 10 kHz	23.57 W	3.45 %
RPP-PWM, f_c = 10 kHz	23.54 W	3.51 %
RZD-PWM, f_c = 10 kHz	23.59 W	3.53 %
G4SRPP-SVPWM, f_c = 10 kHz	24.22 W	3.53 %
G4SRPP-DPWM, f_c = 10 kHz	12.61 W	5.18 %
G4SRPP-DPWM, f_c = 15 kHz	20.13 W	3.28 %

TABLE III

Parameters of the Test IPMSM

Parameters	Value
d-axis inductance	3.4 mH
q-axis inductance	13.95 mH
Permanent magnet flux linkage	0.1 Wb
Pole-pairs	3
Motor speed	2400 r/min
Load torque	22 N·m

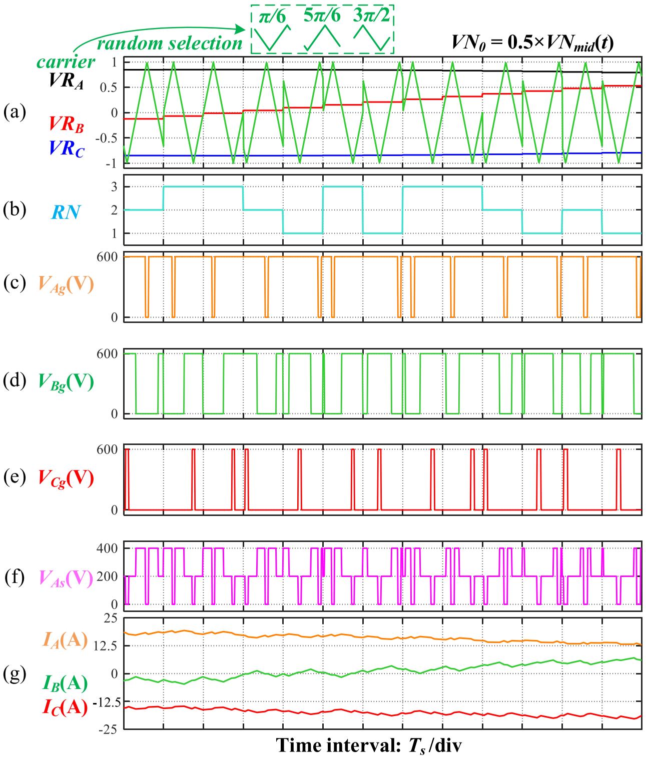

Fig. 11. Simulated waveforms when using G3SRPP-SVPWM with the modulation ratio $a = 0.85$ and the carrier frequency $f_c = 10$ kHz. (a) Intersection between carrier and three-phase reference waves. (b) Random number. (c) *A*-phase output PWM pulse. (d) *B*-phase output PWM pulse. (e) *C*-phase output PWM pulse. (f) *A*-phase voltage. (g) Three-phase currents.

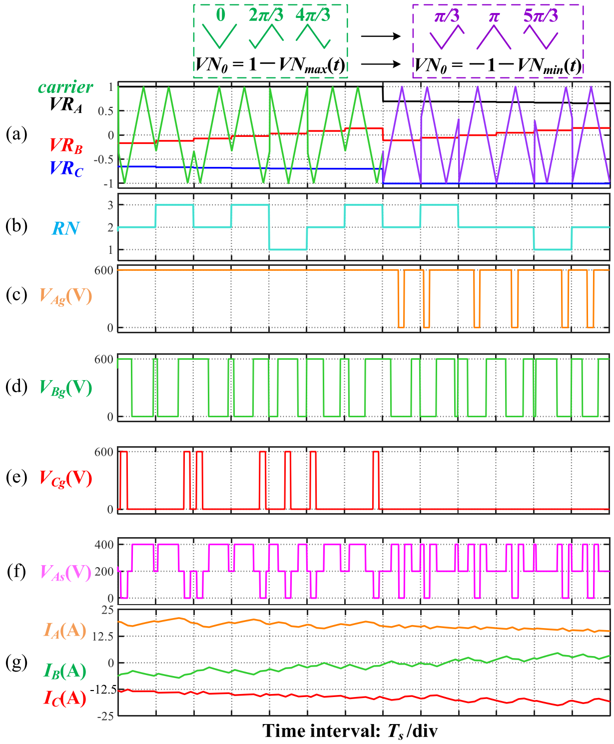

Fig. 12. Simulated waveforms when using the proposed G3SRPP-DPWM with the modulation ratio $a = 0.85$ and the carrier frequency $f_c = 10$ kHz. (a) Intersection between carrier and three-phase reference waves. (b) Random number. (c) *A*-phase output PWM pulse. (d) *B*-phase output PWM pulse. (e) *C*-phase output PWM pulse. (f) *A*-phase voltage. (g) Three-phase currents.

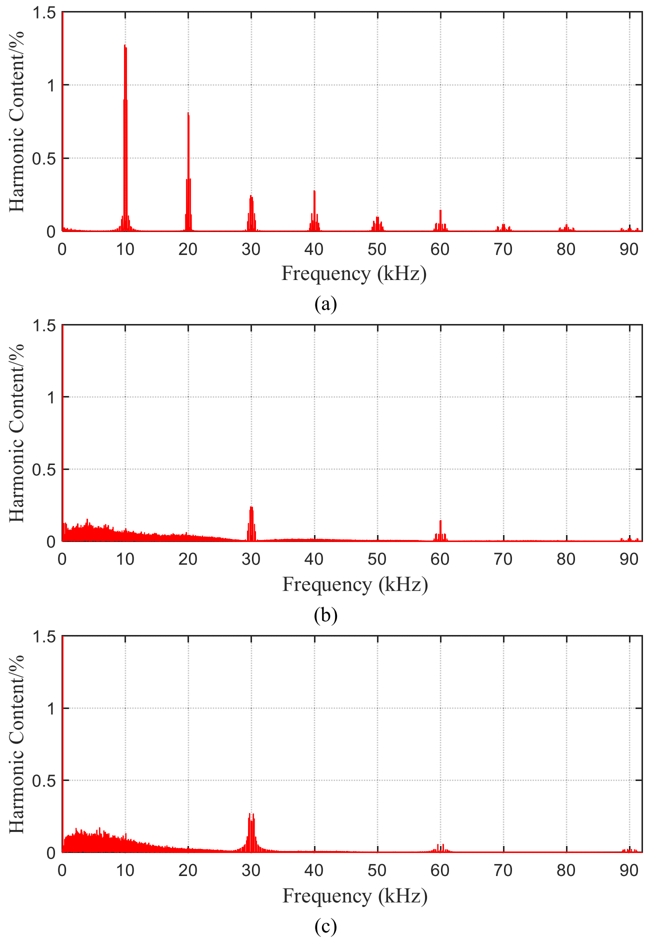

Fig. 13. Spectra of simulated phase current (relative to the fundamental) with the modulation ratio $a = 0.85$ and the carrier frequency $f_c = 10$ kHz. (a) Conventional SVPWM. (b) G3SRPP-SVPWM. (c) G3SRPP-DPWM.

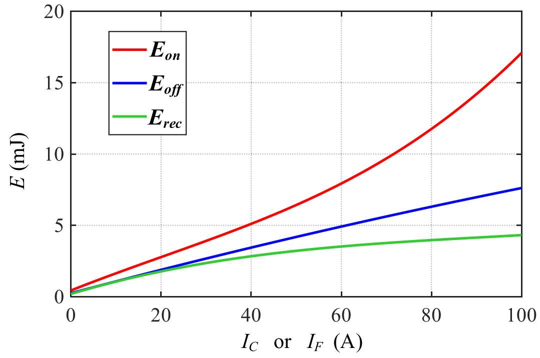

Fig. 14. Switching losses of Si IGBT “Infineon-FF50R12RT4” under inductive load (test condition: Si IGBT at $T_j = 125$ °C, $V_{\mathrm{GE}} = \pm 15$ V, $R_{G\mathrm{on}} = 15\ \Omega$, $R_{G\mathrm{off}} = 15\ \Omega$, and $V_{\mathrm{CE}} = 600$ V).

PWM harmonic component:

$$A_{mn} + jB_{mn} = \frac{1}{2\pi^2} \int_{-\pi}^{\pi} \int_{x_r}^{x_f} V_{dc} e^{j(m(x+\alpha)+ny)} dx dy$$

$$= e^{jm\alpha} \cdot \frac{1}{2\pi^2} \int_{-\pi}^{\pi} \int_{x_r}^{x_f} V_{dc} e^{j(mx+ny)} dx dy$$

$$x_f = \frac{\pi}{2} \left(1 + VR_{\mathrm{GNSRPP-DPWM\_}A}(y)\right)$$

$$x_r = -\frac{\pi}{2} \left(1 + VR_{\mathrm{GNSRPP-DPWM\_}A}(y)\right). \quad (10)$$

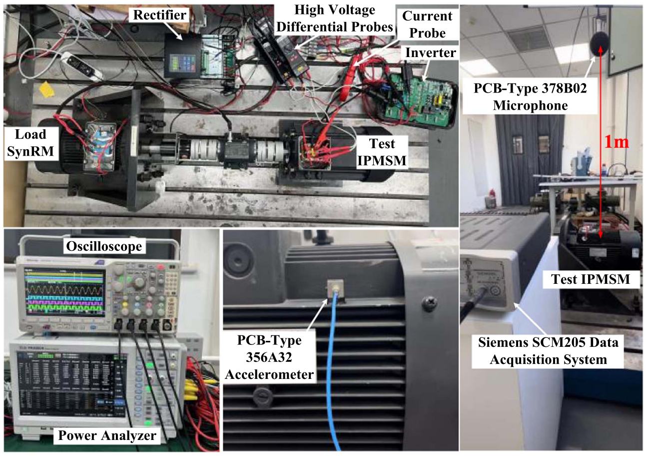

Fig. 15. Photographs of the experimental platform.

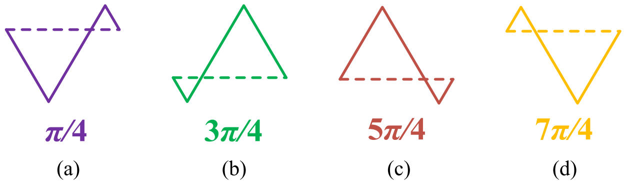

Fig. 16. Fundamental carrier patterns used for random selection in the experiments. (a) *P*1 with $\pi/4$ carrier phase shift. (b) *P*2 with $3\pi/4$ carrier phase shift. (c) *P*3 with $5\pi/4$ carrier phase shift. (d) *P*4 with $7\pi/4$ carrier phase shift.

There is an important multiplication factor $e^{jm\alpha}$ in (10) to explain the dominant PWM harmonics dispersion. Given that the proposed method randomly selects one of the *N* fundamental carrier patterns with the carrier phase shift angles of $\alpha_1, \alpha_2, \ldots,$ and α_N (each pair of them is separated by the phase-shift of $\pi/2$ or its multiple) for every carrier period, the harmonic dispersion coefficient (HDC) is determined using complex vectors as follows:

$$\mathrm{HDC} = \left| \frac{1}{N} \cdot \sum_{i=1}^{N} e^{j \cdot m\alpha_i} \right|$$

$$= \left| \frac{1}{N} \cdot \sum_{i=1}^{N} e^{j \cdot (i-1) \times \frac{2m\pi}{N}} \right| = \begin{cases} 0, m \neq Nk \\ 1, m = Nk \end{cases} \quad (11)$$

where k is a non-negative integer. When $m \neq Nk$, the phase differences among the complex vectors enable mutual cancellation, resulting in the HDC of 0. Conversely, when $m = Nk$, the alignment of complex vectors results in the HDC of 1. This indicates that the proposed method significantly disperses all dominant PWM harmonics, except in cases where $m = Nk$.

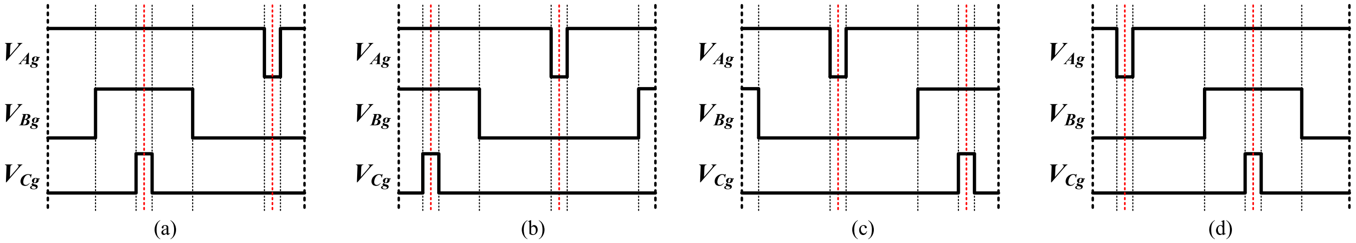

(a) (b) (c) (d)

Fig. 17. Diagram of three-phase output PWM pulses in sector I during one carrier period when $VN_0(t) = 0.5 \times VN_{\text{mid}}(t)$. (a) $P1$ with $\pi/4$ carrier phase shift. (b) $P2$ with $3\pi/4$ carrier phase shift. (c) $P3$ with $5\pi/4$ carrier phase shift. (d) $P4$ with $7\pi/4$ carrier phase shift.

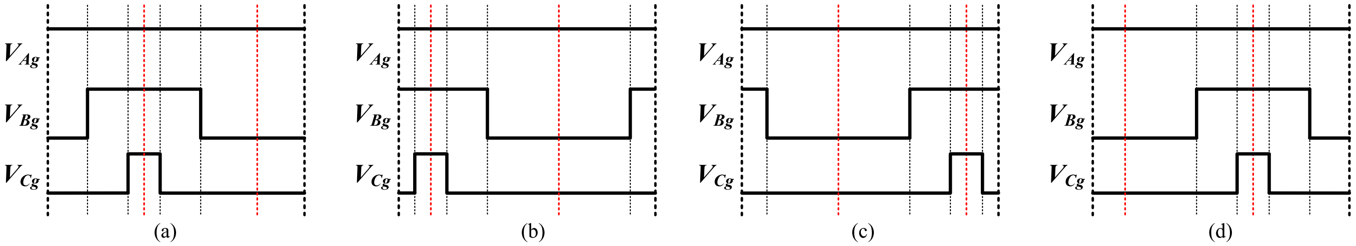

(a) (b) (c) (d)

Fig. 18. Diagram of three-phase output PWM pulses in sector I during one carrier period when $VN_0(t) = 1 - VN_{\max}(t)$. (a) $P1$ with $\pi/4$ carrier phase shift. (b) $P2$ with $3\pi/4$ carrier phase shift. (c) $P3$ with $5\pi/4$ carrier phase shift. (d) $P4$ with $7\pi/4$ carrier phase shift.

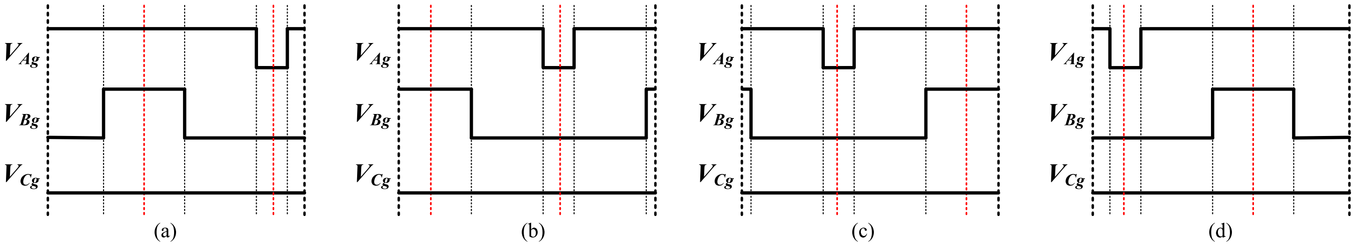

(a) (b) (c) (d)

Fig. 19. Diagram of three-phase output PWM pulses in sector I during one carrier period when $VN_0(t) = -1 - VN_{\min}(t)$. (a) $P1$ with $\pi/4$ carrier phase shift. (b) $P2$ with $3\pi/4$ carrier phase shift. (c) $P3$ with $5\pi/4$ carrier phase shift. (d) $P4$ with $7\pi/4$ carrier phase shift.

TABLE IV
INVERTER POWER LOSSES AND PHASE CURRENT THD OF DIFFERENT STRATEGIES

Modulation Strategies	Inverter Power Losses	Phase Current THD
Conventional SVPWM, f_c = 8 kHz	182.4 W	4.84 %
RPP-SVPWM, f_c = 8 kHz	182.2 W	4.93 %
RZD-SVPWM, f_c = 8 kHz	182.6 W	4.90 %
G4SRPP-SVPWM, f_c = 8 kHz	185.1 W	4.92 %
G4SRPP-DPWM, f_c = 12 kHz	169.5 W	4.58 %

V. SIMULATIONS AND ANALYSIS

This Section takes G3SRPP-DPWM as the example to show. In MATLAB/Simulink, a three-phase two-level VSI has been modeled using regularly sampled modulation. Simulations relevant to this model are conducted under the specified conditions, with key parameters given in Table I.

A. Time- and Frequency-Domain Waveforms

Taking the modulation ratio $a = 0.85$ and sector I as the example to observe, Figs. 10, 11, and 12 show the key time-domain waveform for the conventional SVPWM, G3SRPP-SVPWM, and the proposed G3SRPP-DPWM, respectively. The modulation ratio of 0.85 is higher than $\frac{4}{3\sqrt{3}}$, thereby completely avoiding simultaneous multiphase switching operations, as detailed in the derivations of Section IV-C.

Specifically, as shown in Figs. 10(a), 11(a), and 12(a), the intersection between the carrier wave and the three-phase reference waves (VR_A, VR_B, and VR_C) is crucial to the functioning of PWM technology. Three-phase reference waves are updated once every carrier period to simulate the situation of regularly sampled modulation in real digital control applications. For conventional SVPWM, the carrier-phase shift angle of the fundamental carrier pattern is 0. For G3SRPP-SVPWM, the carrier-phase shift angles of the three fundamental carrier patterns are “$\pi/6$, $5\pi/6$, and $3\pi/2$”. For the proposed G3SRPP-DPWM, the carrier-phase shift angles of the three fundamental carrier patterns are “0, $2\pi/3$ and $4\pi/3$” for “$VN_0(t) = 1 - VN_{\max}(t)$” injection, and “$\pi/3$, π and $5\pi/3$” for “$VN_0(t) = -1 - VN_{\min}(t)$” injection. The carrier wave in Figs. 10(a), 11(a), and 12(a) is composed of a sequence of fundamental carrier patterns determined by the generated random numbers, as shown in Figs. 10(b), 11(b), and 12(b).

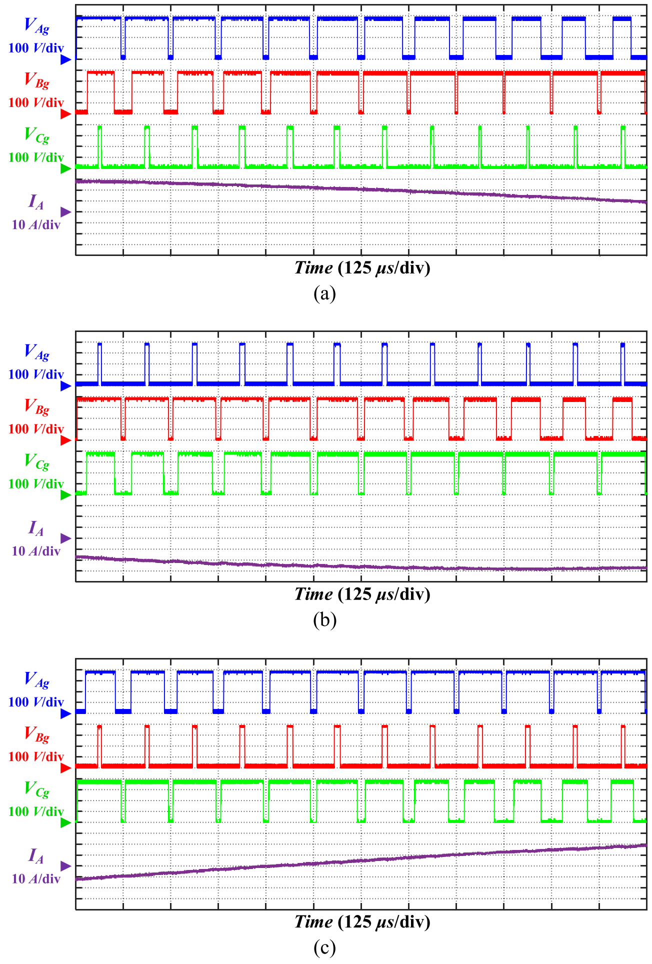

Fig. 20. Experimental waveforms of three-phase output PWM pulses and *A*-phase current during different sectors when using the conventional SVPWM. (a) Sectors I and II. (b) Sectors III and IV. (c) Sectors V and VI.

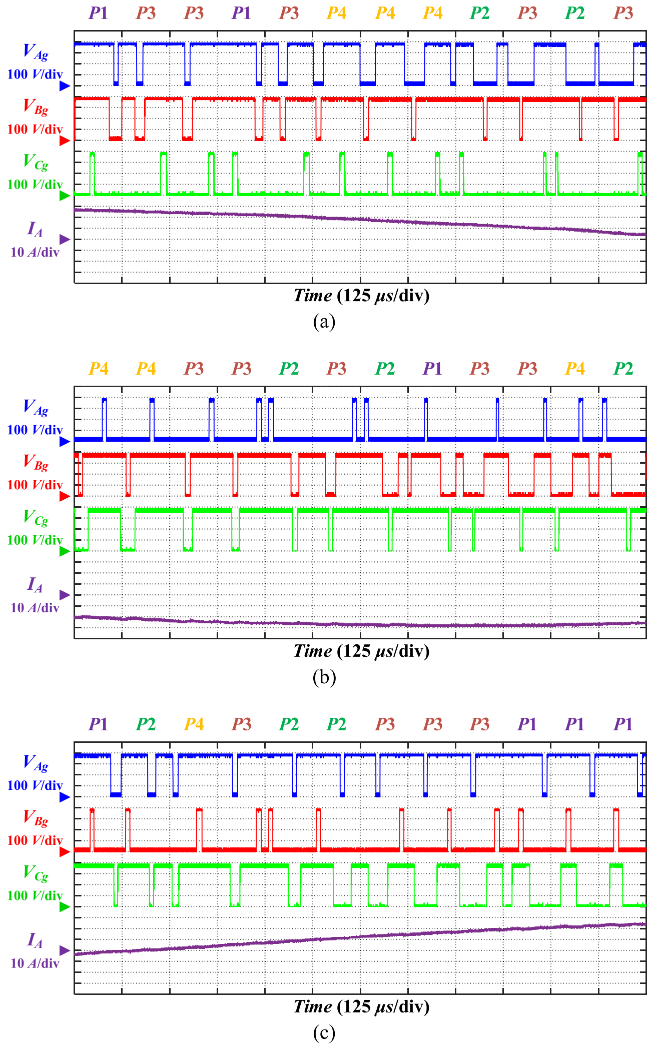

Fig. 21. Experimental waveforms of three-phase output PWM pulses and *A*-phase current during different sectors when using G4SRPP-SVPWM. (a) Sectors I and II. (b) Sectors III and IV. (c) Sectors V and VI.

As shown in Figs. 10(c)–(e), 11(c)–(e), and 12(c)–(e), three-phase output PWM pulses (V_{Ag}, $V_{Bg,}$ and V_{Cg}) are generated from the intersection between the carrier wave and the three-phase reference waves.

Consequently, as illustrated in Figs. 10(g), 11(g), and 12(g), the three-phase current ripples differ significantly among various PWM strategies.

Spectrum analysis is conducted as follows. Fig. 13(a)–(c) shows the spectra (relative to fundamental) of phase current for conventional SVPWM, G3SRPP-SVPWM and the proposed G3SRPP-DPWM, respectively. It is evident that both G3SRPP-SVPWM and G3SRPP-DPWM can significantly disperse the ($3k + 1$)th and ($3k + 2$)th PWM harmonics, whereas conventional SVPWM leads to numerous discrete PWM harmonic peaks near the carrier frequency and its multiples.

B. Output Waveform Quality

THD of phase current is used to evaluate the output waveform quality of different modulation strategies. The comparison of abovementioned strategies is given in Table II. Although the proposed G3SRPP-DPWM with $f_c = 10$ kHz has inferior output waveform quality compared to both G3SRPP-SVPWM and conventional SVPWM with $f_c = 10$ kHz, the proposed G3SRPP-DPWM with $f_c = 15$ kHz has better output waveform quality than both G3SRPP-SVPWM and conventional SVPWM with $f_c = 10$ kHz.

C. Switching Power Losses

Taking the device "Infineon-FF50R12RT4" as an example to analyze, its switching loss behavior extracted from datasheets is given in Fig. 14. These extracted curves are saved in Simulink, and during the simulation, the corresponding switching losses can be obtained according to the instantaneous current values at the moment of switching operation, and finally the switching power losses of different modulation strategies can be obtained as given in Table II. It can be clearly seen that the proposed G3SRPP-DPWM has the smallest switching power losses compared with both conventional SVPWM and G3SRPP-SVPWM. Therefore, with the use of the proposed G3SRPP-DPWM, the

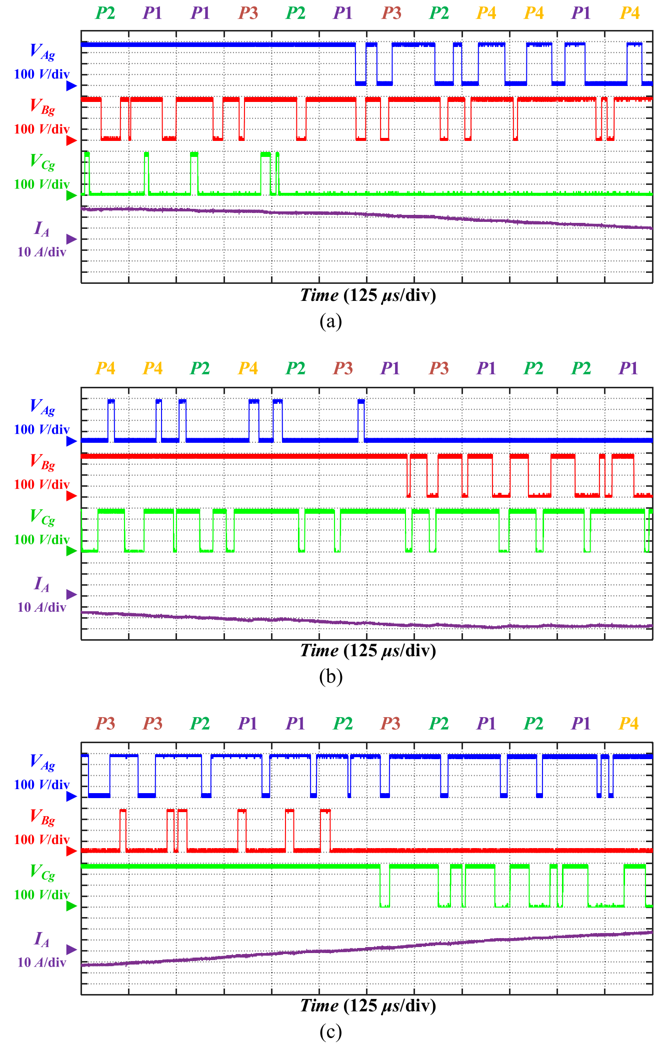

(a)

(b)

(c)

Fig. 22. Experimental waveforms of three-phase output PWM pulses and A-phase current during different sectors when using the proposed G4SRPP-DPWM. (a) Sectors I and II. (b) Sectors III and IV. (c) Sectors V and VI.

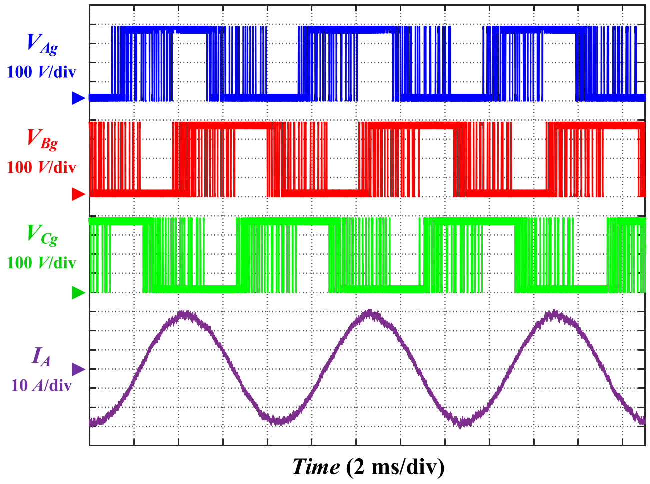

Fig. 23. Experimental waveforms of three-phase output PWM pulses and A-phase current over three fundamental periods when using the proposed G4SRPP-DPWM.

carrier frequency can be further increased, and the output waveform quality can be further improved.

VI. EXPERIMENTAL RESULTS AND ANALYSIS

Experiments take G4SRPP-DPWM as the example to analyze.

Fig. 15 shows a sensorless-controlled interior permanent magnet synchronous motor (IPMSM) drive system developed to validate the effectiveness of the proposed G4SRPP-DPWM. The parameters of the IPMSM sensorless drive system are given in Table III. The carrier frequency f_c is set to 8 kHz. TMS320F280025 DSP chip serves as the microcontroller unit for implementing the control algorithm. Three-phase output PWM pulses are monitored using high-voltage differential probes, phase currents are measured with current probes, and inverter power losses are measured with PA5000H power analyzer. It is important to clarify that the proposed method, aimed at eliminating simultaneous multiphase switching operations, is influenced only by the modulation ratio. In motor control applications, key factors affecting the PWM strategy's modulation ratio include the dc-link voltage, motor speed, and load torque. In this experiment, the dc-link voltage is set at 380V, and the motor operates at 2400 r/min under a load torque of 22 N·m. Under these conditions, the modulation ratio $a \approx 0.9$, which is higher than $\frac{\sqrt{3}}{2}$. According to the derivations in Section IV-C, as long as the modulation ratio is higher than $\frac{\sqrt{3}}{2}$, using G4SRPP-DPWM can completely avoid simultaneous multiphase switching operations. Therefore, the experiment employs G4SRPP-DPWM for validation.

A. Observation of Time-Domain Waveforms

For the conventional SVPWM, the carrier pattern during each carrier period has a carrier phase shift angle of 0. For both G4SRPP-SVPWM and the proposed G4SRPP-DPWM, the fundamental carrier pattern group consists of four carrier patterns with the carrier phase shift angles of "$\pi/4$", "$3\pi/4$", "$5\pi/4$," and "$7\pi/4$," as shown in Fig. 16.

When using G4SRPP-SVPWM, the diagrams of the three-phase output PWM pulses corresponding to the four fundamental carrier patterns are illustrated in Fig. 17 for easy annotation in experimental waveforms. The red dashed lines represent the center alignment lines of the three-phase output PWM pulses. For convenience, only the diagram in sector I $(VR_A > VR_B > VR_C)$ is shown. Similarly, when using G4SRPP-DPWM, the diagrams when the injected zero-sequence voltages are respectively " $VN_0 = 1 - VN_{\max}(t)$" and " $VN_0 = -1 - VN_{\min}(t)$" are shown in Figs. 18 and 19.

For conventional SVPWM, G4SRPP-SVPWM and the proposed G4SRPP-DPWM, Figs. 20, 21, and 22 show their experimental waveforms of three-phase output PWM pulses and A-phase current. The time-axis interval is the carrier period. The carrier phase shift angles of "$\pi/4$," "$3\pi/4$," "$5\pi/4$," and "$7\pi/4$" are marked as "$P1$," "$P2$," "$P3$," and "$P4$" respectively at the top of the figures. It is evident that the experimental waveforms of the final output PWM pulses in Fig. 21 are obtained by the

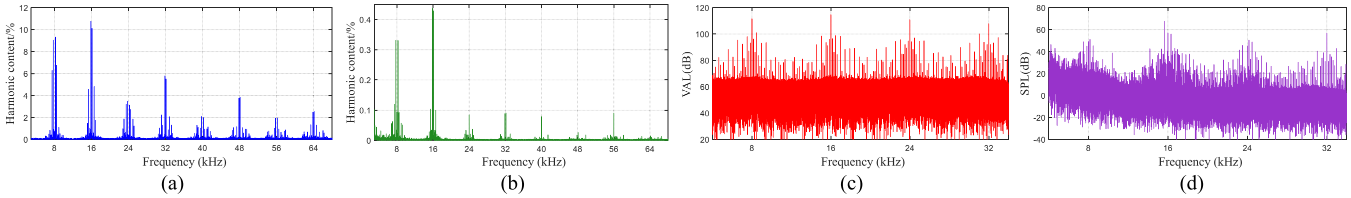

(a) (b) (c) (d)

Fig. 24. Experimental spectrum analysis when using the conventional SVPWM. (a) V_{As}. (b) i_A. (c) Vibration acceleration level. (d) Sound pressure level.

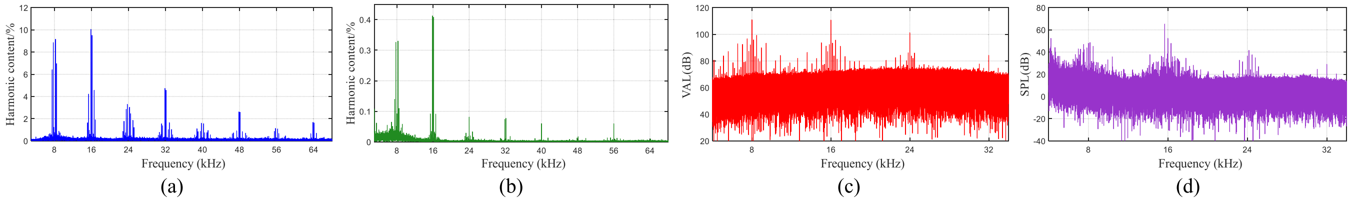

(a) (b) (c) (d)

Fig. 25. Experimental spectrum analysis when using the traditional RPP-PWM. (a) V_{As}. (b) i_A. (c) Vibration acceleration level. (d) Sound pressure level.

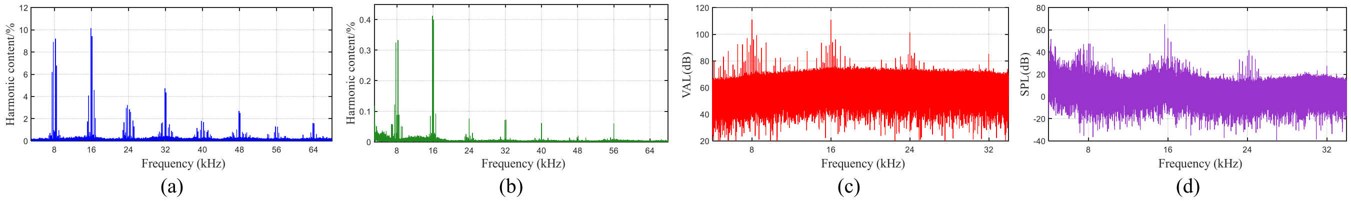

(a) (b) (c) (d)

Fig. 26. Experimental spectrum analysis when using the traditional RZD-PWM. (a) V_{As}. (b) i_A. (c) Vibration acceleration level. (d) Sound pressure level.

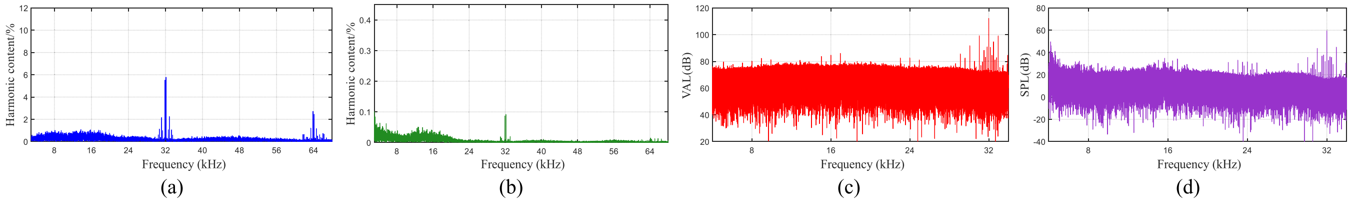

(a) (b) (c) (d)

Fig. 27. Experimental spectrum analysis when using G4SRPP-SVPWM. (a) V_{As}. (b) i_A. (c) Vibration acceleration level. (d) Sound pressure level.

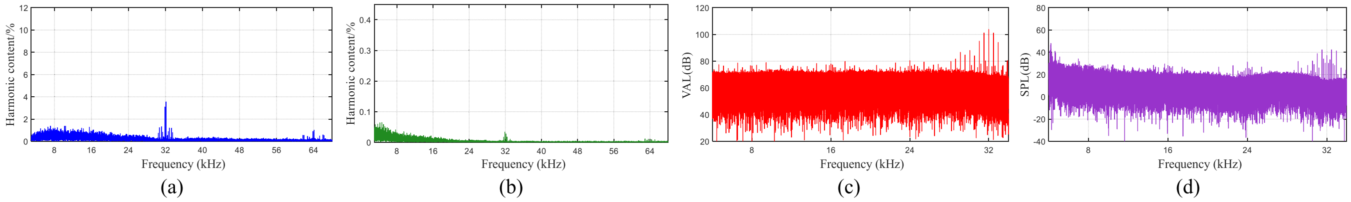

(a) (b) (c) (d)

Fig. 28. Experimental spectrum analysis when using the proposed G4SRPP-DPWM. (a) V_{As}. (b) i_A. (c) Vibration acceleration level. (d) Sound pressure level.

random combination of diagrams in Fig. 17, and those in Fig. 22 are obtained by the random combination of diagrams in Figs. 18 or 19.

B. Inverter Performance

This part shows the comparison of inverter power losses and phase current THD for different modulation strategies.

Fig. 23 shows the experimental waveforms of three-phase output PWM pulses and *A*-phase current over three fundamental periods when using the proposed G4SRPP-DPWM. It can be clearly seen from the V_{Ag} and I_A waveforms that when the *A*-phase current approaches the maximum magnitudes, the *A*-phase switch will not operate, thereby reducing switching power losses.

Moreover, it can be seen from Table IV that compared with the conventional SVPWM, G4SRPP-SVPWM slightly increases the

TABLE V
COMPARISON OF DIFFERENT RANDOM PULSEWIDTH MODULATION STRATEGIES

	RCD-PWM and RZD-PWM	RCF-PWM	NSRPP-SVPWM	GNSRPP-SVPWM With Even Number N	The proposed GNSRPP-DPWM With $N \geq 3$
Harmonic Reduction Performance	Bad	Average	Good	Good	Good
Sampling Frequency	Constant	Variable	Constant	Constant	Constant
Closed-Loop Control System	Applicable	Not Applicable	Applicable	Applicable	Applicable
Applicable Modulation Ratio Range	Low Range	Full Range	Full Range	$a \geq \frac{2}{\sqrt{3}} \times \left(2 \cdot \left\lvert\frac{\pi/N}{\pi} - 1\right\rvert - 1\right)$	$a \geq \frac{2}{\sqrt{3}} \times \left(2 \cdot \left\lvert\frac{\pi/N}{2\pi} - 1\right\rvert - 1\right)$
Simultaneous Multiphase Switching	No	No	Yes	No	No
Phase Current THD	Comparison Base Value	Similar	Similar	Similar	Reduced
Switching Power Loss	Comparison Base Value	Similar	Significantly Increased	Slightly Increased	Reduced

inverter power losses and phase current THD, while the proposed G4SRPP-DPWM with the carrier frequency $f_c = 12$ kHz reduces the inverter power losses and the phase current THD. Thus, the proposed G4SRPP-DPWM improves the inverter performance.

C. Implementation of Spectrum Analysis

For different modulation strategies, Figs. 24–28 show their key spectrum analysis. The vibration acceleration level (VAL), denoted in decibels (dB), is calculated using the formula

$$\mathrm{VAL} = 20\log_{10}\frac{A}{A_o} \tag{12}$$

where $A_o = 1 \times 10^{-6}$ m/s^2 represents the reference acceleration, while A denotes to the measured acceleration.

The sound pressure level (SPL), denoted in dB, is calculated using the formula

$$\mathrm{SPL} = 20\log_{10}\frac{P}{P_o} \tag{13}$$

where $P_o = 2 \times 10^{-5}$ Pa represents the reference sound pressure, and P denotes to the measured sound pressure. For SPL spectrum analysis, the test IPMSM operates with no load to avoid the noise from the accompanying motor.

Measurements of VAL and SPL are conducted using the Siemens SCM205 Data Acquisition System, a PCB-type 356A32 accelerometer and a PCB-type 378B02 microphone. As shown in Fig. 15, the accelerometer is mounted on the motor casing, and the microphone is placed at a distance of 1 m from the noise source with the microphone axis pointing towards the test motor.

Fig. 24 illustrates that using conventional SVPWM results in discrete PWM harmonic peaks around the carrier frequency and its integer multiples.

Figs. 25 and 26 present the spectrum analysis for traditional RPP-PWM and RZD-PWM, which, due to the short durations of the zero-voltage vectors, exhibit poor PWM harmonic dispersion performance.

As shown in Figs. 27 and 28, G4SRPP-SVPWM and the proposed G4SRPP-DPWM effectively spread the $(4k + 1)$th, $(4k + 2)$th, and $(4k + 3)$th PWM harmonics.

It is worth noting that when using RCF-PWM, the test IPMSM cannot be started because the random sampling frequency affects the sensorless closed-loop control algorithm.

VII. CONCLUSION

This article proposed GNSRPP-DPWM to significantly disperse dominant PWM harmonics and improve inverter performance at high modulation ratios. The comparison of different RPWM strategies is given in Table V. It is verified by mathematical analysis, simulations and experiments that the proposed GNSRPP-DPWM not only significantly reduces the dominant discrete PWM harmonic peaks in the spectrum of phase voltage, phase current, VAL and SPL, but also reduces harmonic distortion and inverter power losses. Besides, the proposed method maintains constant sampling frequency and is therefore applicable in closed-loop control systems. However, as previously mentioned, the proposed GNSRPP-DPWM fully prevents simultaneous multiphase switching operations and enhances inverter performance only at high modulation ratios. Caution is advised when applying it in applications with low modulation ratios, as simultaneous multiphase switching operations may occur.

REFERENCES

[1] W. Liang, J. Wang, P. C.-K. Luk, W. Fang, and W. Fei, “Analytical modeling of current harmonic components in PMSM drive with voltage-source inverter by SVPWM technique,” *IEEE Trans. Energy Convers.*, vol. 29, no. 3, pp. 673–680, Sep. 2014.

[2] D. J. Hogan, F. J. Gonzalez-Espin, J. G. Hayes, G. Lightbody, and R. Foley, “An adaptive digital-control scheme for improved active power filtering under distorted grid conditions,” *IEEE Trans. Ind. Electron.*, vol. 65, no. 2, pp. 988–999, Feb. 2018.

[3] F. Blaabjerg and K. Ma, “Future on power electronics for wind turbine systems,” *IEEE J. Emerg. Sel. Topics Power Electron.*, vol. 1, no. 3, pp. 139–152, Sep. 2013.

[4] A. M. Hava, R. J. Kerkman, and T. A. Lipo, “Simple analytical and graphical methods for carrier-based PWM-VSI drives,” *IEEE Trans. Power Electron.*, vol. 14, no. 1, pp. 49–61, Jan. 1999.

[5] D. Grahame Holmes and T. A. Lipo, “Zero space vector placement modulation strategies,” in *Pulse Width Modulation for Power Converters: Principles and Practice*. Hoboken, NJ, USA: Wiley, 2003, pp. 259–336.

[6] O. Ojo, “The generalized discontinuous PWM scheme for three-phase voltage source inverters,” *IEEE Trans. Ind. Electron.*, vol. 51, no. 6, pp. 1280–1289, Dec. 2004.

[7] T. D. Nguyen, J. Hobraiche, N. Patin, G. Friedrich, and J.-P. Vilain, “A direct digital technique implementation of general discontinuous pulse width modulation strategy,” *IEEE Trans. Ind. Electron.*, vol. 58, no. 9, pp. 4445–4454, Sep. 2011.

[8] S.-L. An, X.-D. Sun, Q. Zhang, Y.-R. Zhong, and B.-Y. Ren, “Study on the novel generalized discontinuous SVPWM strategies for three-phase voltage source inverters,” *IEEE Trans. Ind. Inform.*, vol. 9, no. 2, pp. 781–789, May 2013.

[9] D. Jiang and F. Wang, "Variable switching frequency PWM for three-phase converters based on current ripple prediction," *IEEE Trans. Power Electron.*, vol. 28, no. 11, pp. 4951–4961, Nov. 2013.

[10] Y. Huang, Y. Xu, Y. Li, G. Yang, and J. Zou, "PWM frequency voltage noise cancelation in three-phase VSI using the novel SVPWM strategy," *IEEE Trans. Power Electron.*, vol. 33, no. 10, pp. 8596–8606, Oct. 2018.

[11] W. Liang, P. C.-K. Luk, and W. Fei, "Analytical investigation of sideband electromagnetic vibration in integral-slot PMSM drive with SVPWM technique," *IEEE Trans. Power Electron.*, vol. 32, no. 6, pp. 4785–4795, Jun. 2017.

[12] A. Ruiz-Gonzalez, F. Vargas-Merino, J. R. Heredia-Larrubia, M. J. Meco-Gutierrez, and F. Perez-Hidalgo, "Application of slope PWM strategies to reduce acoustic noise radiated by inverter-fed induction motors," *IEEE Trans. Ind. Electron.*, vol. 60, no. 7, pp. 2555–2563, Jul. 2013.

[13] Z. Zhang, L. Wei, P. Yi, Y. Cui, P. S. Murthy, and A. M. Bazzi, "Conducted emissions suppression of active front end (AFE) drive based on random switching frequency PWM," *IEEE Trans. Ind. Appl.*, vol. 56, no. 6, pp. 6598–6607, Nov./Dec. 2020.

[14] K. Mainali and R. Oruganti, "Conducted EMI mitigation techniques for switch-mode power converters: A survey," *IEEE Trans. Power Electron.*, vol. 25, no. 9, pp. 2344–2356, Sep. 2010.

[15] A. Peyghambari, A. Dastfan, and A. Ahmadyfard, "Selective voltage noise cancellation in three-phase inverter using random SVPWM," *IEEE Trans. Power Electron.*, vol. 31, no. 6, pp. 4604–4610, Jun. 2016.

[16] H. Li, Z. Yang, B. Wang, V. G. Agelidis, and B. Zhang, "On thermal impact of chaotic frequency modulation SPWM techniques," *IEEE Trans. Ind. Electron.*, vol. 64, no. 3, pp. 2032–2043, Mar. 2017.

[17] J. Xu, Z. Nie, and J. Zhu, "Characterization and selection of probability statistical parameters in random slope PWM based on uniform distribution," *IEEE Trans. Power Electron.*, vol. 36, no. 1, pp. 1184–1192, Jan. 2021.

[18] F. Bu, T. Pu, W. Huang, and L. Zhu, "Performance and evaluation of five-phase dual random SVPWM strategy with optimized probability density function," *IEEE Trans. Ind. Electron.*, vol. 66, no. 5, pp. 3323–3332, May 2019.

[19] Y. Wu, J. Xu, T. B. Soeiro, M. Stecca, and P. Bauer, "Optimal periodic variable switching PWM for harmonic performance enhancement in grid-connected voltage source converters," *IEEE Trans. Power Electron.*, vol. 37, no. 6, pp. 7247–7262, Jun. 2022.

[20] Z. Ji, S. Cheng, Q. Ren, X. Li, Y. Lv, and D. Wang, "The effects and mechanisms of periodic-carrier-frequency PWM on vibrations of multiphase permanent magnet synchronous motors," *IEEE Trans. Power Electron.*, vol. 38, no. 7, pp. 8696–8706, Jul. 2023.

[21] Y. Yang, W. Song, Y. Ge, and P. Wheeler, "A Markov chain random asymmetrical SVPWM method to suppress high-frequency harmonics of output current in an IMC-PMSM system," *IEEE Trans. Power Electron.*, vol. 39, no. 1, pp. 135–148, Jan. 2024.

[22] J. Xu, Z. Ouyang, Y. Dong, and Z. Nie, "Spectrum-dispersion effects of random triangular carrier wave SVPWM for NPC three-level inverters," *IEEE Trans. Ind. Electron.*, vol. 71, no. 7, pp. 7756–7765, Jul. 2024.

[23] F. Bu et al., "Analysis and performance of five-phase piecewise-random-switching-frequency space vector pulse width modulation," *IEEE Trans. Energy Convers.*, vol. 36, no. 3, pp. 2339–2347, Sep. 2021.

[24] Y.-S. Lai, Y.-T. Chang, and B.-Y. Chen, "Novel random-switching PWM technique with constant sampling frequency and constant inductor average current for digitally controlled converter," *IEEE Trans. Ind. Electron.*, vol. 60, no. 8, pp. 3126–3135, Aug. 2013.

[25] A. M. Trzynadlowski, K. Borisov, Y. Li, and L. Qin, "A novel random PWM technique with low computational overhead and constant sampling frequency for high-volume, low-cost applications," *IEEE Trans. Power Electron.*, vol. 20, no. 1, pp. 116–122, Jan. 2005.

[26] M. M. Bech, F. Blaabjerg, and J. K. Pedersen, "Random modulation techniques with fixed switching frequency for three-phase power converters," *IEEE Trans. Power Electron.*, vol. 15, no. 4, pp. 753–761, Jul. 2000.

[27] Y.-C. Lim, Y.-G. Jung, S.-Y. Oh, and J.-G. Kim, "A two-phase separately randomized pulse position PWM (SRP-PWM) scheme with low switching noise characteristics over the entire modulation index," *IEEE Trans. Power Electron.*, vol. 27, no. 1, pp. 362–369, Jan. 2012.

[28] R. L. Kirlin, C. Lascu, and A. M. Trzynadlowski, "Shaping the noise spectrum in power electronic converters," *IEEE Trans. Ind. Electron.*, vol. 58, no. 7, pp. 2780–2788, Jul. 2011.

[29] P. Zhang, S. Wang, and Y. Li, "Performance and analysis of N-state random pulse position SVPWM with constant sampling frequency," *IEEE Trans. Power Electron.*, vol. 37, no. 11, pp. 13606–13625, Nov. 2022.

[30] A. M. Hava and E. Ün, "A high-performance PWM algorithm for common-mode voltage reduction in three-phase voltage source inverters," *IEEE Trans. Power Electron.*, vol. 26, no. 7, pp. 1998–2008, Jul. 2011.

[31] A. M. Hava and E. Ün, "Performance analysis of reduced common-mode voltage PWM methods and comparison with standard PWM methods for three-phase voltage-source inverters," *IEEE Trans. Power Electron.*, vol. 24, no. 1, pp. 241–252, Jan. 2009.

[32] A. M. Hava, N. O. Cetin, and E. Un, "On the contribution of PWM methods to the common mode (leakage) current in conventional three-phase two-level inverters as applied to AC motor drives," in *Proc. IEEE Ind. Appl. Soc. Annu. Meeting*, 2008, pp. 1–8.

[33] J. Xu, J. Han, Y. Wang, M. Ali, and H. Tang, "High-frequency SiC three-phase VSIs with common-mode voltage reduction and improved performance using novel tri-state PWM method," *IEEE Trans. Power Electron.*, vol. 34, no. 2, pp. 1809–1822, Feb. 2019.

[34] P. Zhang, S. Wang, and Y. Li, "Three-phase two-level VSIs with significant PWM harmonics dispersion and improved performance using generalized N-state random pulse position SVPWM with constant sampling frequency," *IEEE Trans. Power Electron.*, vol. 39, no. 1, pp. 1394–1409, Jan. 2024.

Peiran Zhang received the B.S. degree in electrical engineering from Shandong University, Jinan, China, in 2020. He is currently working toward the Ph.D. degree in electrical engineering with the Department of Electrical Engineering, Tsinghua University, Beijing, China.

His main research interests include power converter, motor drive, and sensorless control.

Shanming Wang (Senior Member, IEEE) received the B.S. and M.S. degrees in electrical engineering from Nanchang University, Nanchang, China, in 1993 and 1996, respectively, and the Ph.D. degree in electrical engineering from the Department of Electrical Engineering, Tsinghua University, Beijing, China, in 2001.

In 2001, he was with the Department of Electrical Engineering, Tsinghua University, where he is currently a Professor. His research interests include the analysis and control of electric machines, vibration analysis of electrical machines, hybrid excitation PM machines, the simulation of ac machines and systems, and fault analysis for electric machines and its protection.

Yituo Li received the Ph.D. degree in electrical engineering from Tsinghua University, Beijing, China, in 2013.

He is currently a Research Staff with Tsinghua University. His main interests include high-performance ac drives and sensorless control.